Check for updates

Advanced Functional Materials

ADVANCED FUNCTIONAL MATERIALS
www.afm-journal.de

RESEARCH ARTICLE

Unlocking Ultrafast Charging: Synergizing Embedded Pseudocapacitive Domains and Flexible Lattice Dynamics in Off-Stoichiometric $LiTi_2(PO_4)_3$ Anodes

Chungsun Oh[1] | Sieun An[1] | Hoyoung Suh[2] | Jiyoung Youn[1] | Geunhong Park[1] | Dohoon Kim[1] | Heechul Jung[1] | Jaewon Jang[3,4] | Yong-Il Kim[3] | Dongwook Han[1]

[1]Department of Future Energy Convergence, Seoul National University of Science and Technology, Seoul, Republic of Korea | [2]Advanced Analysis & Data Center, Korea Institute of Science and Technology (KIST), Seoul, Republic of Korea | [3]Non-Destructive Metrology Group, Korea Research Institute of Standards and Science (KRISS), Daejeon, Republic of Korea | [4]Department of Measurement Engineering, University of Science and Technology, Daejeon, Republic of Korea

Correspondence: Yong-Il Kim (yikim@kriss.re.kr) | Dongwook Han (dw.han@seoultech.ac.kr)

Received: 12 December 2025 | **Revised:** 25 April 2026 | **Accepted:** 23 May 2026

Keywords: flexible lattice dynamics | lithium-ion batteries | lithium titanium phosphates | off-stoichiometric engineering | pseudocapacitance | ultrafast charging

ABSTRACT

Overcoming the intrinsic trade-off between particle size and ionic kinetics of active materials is essential for realizing high volumetric energy density, ultrafast-charging lithium-ion batteries. Here, we report a rational design strategy to unlock ultrafast charging capabilities in off-stoichiometric microscale $LiTi_2(PO_4)_3$ (LTP) anodes by synergizing embedded pseudocapacitive domains with flexible lattice dynamics. Through precise Ti-deficiency engineering, TiP_2O_7 domains are induced in situ within the LTP subsurface, creating a cohesive hetero-architecture. These domains serve as high-flux kinetic gateways that lower the activation energy for interfacial Li-ion transfer. Concurrently, the induced lattice flexibility, derived from the rotational degrees of freedom in the P—O—P bridges, accommodates rapid ionic flux and mitigates structural strain, while the robust NASICON framework preserves facile bulk diffusion. Consequently, this architecture circumvents typical kinetic limitations, delivering exceptional rate capability at an aggressive 10C rate for over 250 cycles, even with large secondary particles reaching up to 30 μm. This off-stoichiometry-driven approach establishes a versatile paradigm for developing next-generation high-power energy storage materials, extending its potential to all-solid-state battery applications.

1 | Introduction

The pursuit of smart mobility and high-power electronics has intensified the demand for Li-ion batteries (LIBs) capable of ultrafast and safe charging [1, 2]. However, high-rate operation remains a critical bottleneck, as it often triggers accelerated active material degradation and catastrophic failure, posing significant safety and lifespan concerns [3, 4]. This challenge is particularly acute for the anode materials. During rapid charging, conventional graphite anodes suffer from severe cathodic polarization, leading to hazardous Li-metal plating on their surface [5–7]. Furthermore, pronounced Joule heating, proportional to the square of the applied current, can induce thermal runaway and compromise cell safety [8, 9]. While alternative anode materials like silicon exhibit high capacity, their application is plagued by mechanical pulverization from massive volume changes during cycling [10].

To mitigate these issues, high-voltage anode materials (>1.5 V vs. Li^+/Li), such as spinel $Li_4Ti_5O_{12}$, have emerged as safer

© 2026 Wiley-VCH GmbH

alternatives [11, 12]. Their higher operating potential effectively prevents the Li plating and minimizes the formation of unstable solid-electrolyte interphase (SEI) layers. Nevertheless, state-of-the-art high-voltage transition-metal oxides are often hampered by poor electronic/ionic conductivities and insufficient thermal stability, which limits their power density and long-term reliability under demanding conditions [13–15]. This necessitates a paradigm shift toward new material systems that are intrinsically stable and kinetically efficient.

In this context, polyanionic compounds, particularly those with the Na superionic conductor (NASICON) structure, present a compelling yet underexplored system for fast-charging anode materials [16, 17]. Their rigid, three-dimensional frameworks offer exceptional structural and thermal stability, along with well-defined pathways for rapid Li-ion diffusion. While their high operating voltages and modest theoretical capacities have traditionally been viewed as drawbacks, these characteristics become advantageous for high-power applications where safety, stability, and rate capability take precedence over absolute energy density. To unlock their full potential, however, the key challenge lies in synergistically optimizing two kinetic parameters: facile charge transfer at the electrode-electrolyte interface and rapid Li-ion transport within the bulk crystal structure [18–20].

Herein, we report a pioneering class of off-stoichiometric $LiTi_2(PO_4)_3$ (LTP) anode materials rationally designed to conquer the dual kinetic challenges of bulk diffusion and interfacial transfer within a single, integrated architecture. The NASICON framework of LTP intrinsically serves as a *superhighway* for rapid bulk Li-ion transport and remarkable structural robustness [17, 21–23]. However, resolving the sluggish interfacial kinetics remains critical, as charge-transfer bottlenecks often provoke surface degradation and limit rate capability [24, 25]. To address this, we employ an innovative off-stoichiometric engineering strategy. By deliberately creating a Ti-deficiency, we trigger the in situ formation of TiP_2O_7 (TPO) domains at the LTP particle subsurface. These domains can lower the activation energy for interfacial Li-ion transfer [26, 27]. Specifically, the pyrophosphate $(P_2O_7)^{4-}$ framework possesses inherent structural flexibility derived from the rotational degrees of freedom in its P—O—P bridges [28, 29]. This crystallographic feature allows the TPO domains to act as a *strain buffer*, effectively accommodating lattice mismatch during high-rate Li-ion insertion and thereby mitigating the activation barrier at the interface.

Consequently, these embedded TPO-rich domains function as highly efficient *kinetic boosters*, dramatically accelerating charge transfer at the electrode-electrolyte interface and ensuring uniform Li-ion flux into the LTP particle core. This unique hetero-architecture achieves a remarkable synergy: the pseudocapacitive surface facilitates rapid charge accumulation, while the stable NASICON core provides facile transport and accommodation of Li ions. In this work, we demonstrate that this off-stoichiometry-driven design delivers exceptional high-rate performance and cycling stability, far surpassing conventional anode materials. We elucidate the formation mechanism of the integrated domains and reveal how this strategy unlocks unprecedented charging capabilities, even for commercially relevant, microscale active secondary particles reaching up to 30 μm. This study establishes off-stoichiometric engineering as a powerful and generalizable strategy for creating next-generation, high-power energy storage materials.

TABLE 1 | Chemical compositions and elemental ratios of P-LTP/C and OS-LTP/C determined by ICP-OES analysis.

Samples	P-LTP/C	OS-LTP/C
P/Ti	1.51	1.55
Li/Ti	0.47	0.48
Chemical compositions	$Li_{0.93}Ti_{1.99}(PO_4)_3$	$Li_{0.93}Ti_{1.95}(PO_4)_3$

2 | Results and Discussion

2.1 | Material Characterization

2.1.1 | Validating the Off-Stoichiometric Design

To validate the successful implementation of our off-stoichiometric engineering strategy, the precise chemical compositions and key physical properties of the pristine stoichiometric (hereafter P-LTP/C) and target off-stoichiometric (OS-LTP/C) materials were systematically characterized. The elemental ratios, quantified by inductively coupled plasma-optical emission spectrometry (ICP-OES), provide the first crucial evidence of our design (Table 1). The pristine P-LTP/C exhibited a P/Ti atomic ratio of 1.51, closely matching the theoretical value of 1.5 for stoichiometric LTP. In sharp contrast, the OS-LTP/C sample presented a significantly higher P/Ti ratio of 1.55, unequivocally confirming the successful creation of the intended Ti-deficiency. Both samples showed a similar, slight Li deficiency (Li/Ti ≈ 0.47–0.48), which is commonly observed and attributable to lithium evaporation during high-temperature synthesis. The residual carbon contents, measured by CHNS/O analysis, were determined to be 5.12 and 4.45 wt.% for P-LTP/C and OS-LTP/C, respectively.

Field-emission scanning electron microscopy (FE-SEM) was then employed to compare the morphologies. Both P-LTP/C and OS-LTP/C consist of large, irregular secondary particles reaching up to 30 μm (Figure S1). Energy-dispersive X-ray spectroscopy (EDS) mapping revealed a homogeneous distribution of Ti, P, and O throughout the particles in both samples, with no evidence of elemental segregation at this scale. The median particle size (D_{50}) of OS-LTP/C (≈15.1 μm) is virtually identical to that of the pristine sample (≈15.3 μm, Figure S2). This morphological and distributional similarity is a critical finding; it ensures that any subsequent differences in electrochemical performance can be directly and unambiguously attributed to our compositional engineering (namely, the introduction of off-stoichiometry and the resulting embedded domains) rather than to variations in particle size or elemental distribution.

16163028, 0, Downloaded from https://advanced.onlinelibrary.wiley.com/doi/10.1002/adfm.76250 by Dongwook Han - Seoul National University Of , Wiley Online Library on [01/06/2026]. See the Terms and Conditions (https://onlinelibrary.wiley.com/terms-and-conditions) on Wiley Online Library for rules of use; OA articles are governed by the applicable Creative Commons License

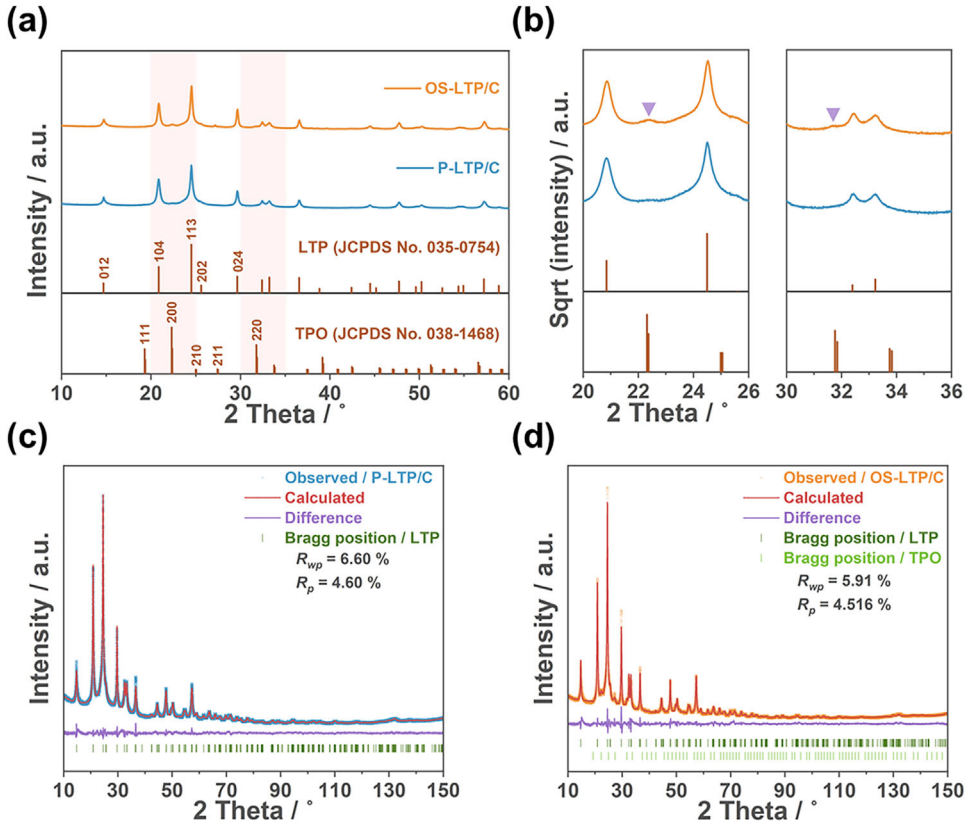

FIGURE 1 | Crystallographic characterization. (a) XRD patterns of P-LTP/C and OS-LTP/C. (b) Magnified views of the 20°–26° and 30°–36° ranges with the intensity plotted on a square root (Sqrt) scale. (c, d) Rietveld refinement profiles for P-LTP/C and OS-LTP/C.

2.1.2 | Structural and Phase Analysis: Evidence of Integrated Hetero-Domains

To elucidate the crystallographic origins of the engineered off-stoichiometry, X-ray diffraction (XRD) analysis was performed. As shown in Figure 1a, the pristine P-LTP/C sample exhibits a single set of well-defined diffraction peaks, all of which are perfectly indexed to the rhombohedral NASICON-type $LiTi_2(PO_4)_3$ (LTP) phase (JCPDS No. 035–0754) [30]. This confirms its phase-pure, stoichiometric nature. In contrast, the XRD pattern of OS-LTP/C reveals the presence of the primary LTP phase alongside several distinct, minor peaks. These additional reflections, such as the prominent peak at $2\theta \approx 22.5°$ (Figure 1b), are characteristic of a cubic TiP_2O_7 (TPO) secondary phase (JCPDS No. 038–1468) [31]. This result provides direct crystallographic evidence that the deliberately introduced Ti-deficiency successfully triggered the in situ formation of TPO domains within the LTP host matrix. The slight broadening of the main diffraction peaks in both samples is attributed to the presence of an amorphous carbon derived from the thermal decomposition of the citric acid precursor.

To gain deeper quantitative insights into the crystal structures, Rietveld refinement was conducted on the XRD data (Figure 1c,d). The refinement of the P-LTP/C pattern converged excellently with a low weighted-profile R-factor (R_{wp}) of 6.6%, confirming its single-phase NASICON structure. For the OS-LTP/C sample, a two-phase model incorporating both the rhombohedral LTP (space group: *R*-3*c*) and cubic TPO (space group: *Pa*-3) phases was employed. This model also yielded an excellent fit (R_{wp} = 5.91%), further validating our structural hypothesis. Crucially, the quantitative phase analysis revealed that the OS-LTP/C material consists of approximately 96.2 wt.% LTP and 3.8 wt.% TPO. The refined crystallographic parameters, including the lattice constants for both samples, are summarized in Table S1. The subtle differences in the lattice parameters between P-LTP/C and the LTP phase in OS-LTP/C suggest a slight structural strain induced by the embedded TPO domains.

For atomic-scale visualization of these bulk crystallographic findings, the STEM image of OS-LTP/C reveals depth-dependent structural variations from the surface to the bulk (Figure 2a). The corresponding selected area electron diffraction (SAED) pattern (Figure 2b) exhibits concentric diffraction rings, indicating the polycrystalline characteristics of OS-LTP/C. Notably, one of the diffraction rings cannot be indexed to any interplanar spacing of the LTP phase; rather, it corresponds exactly to the (200) plane of TPO. Figure 2c presents the HR-TEM image of OS-LTP/C, comparing representative bulk (region i) and subsurface (region ii) areas. The fast Fourier transform (FFT) pattern obtained from region ii directly validates the presence of distinct cubic TPO domains in the subsurface.

Furthermore, considering that Ti-deficiency is accompanied by oxygen vacancies (Table S1), it is inferred that the TPO phase is preferentially concentrated in the subsurface regions, which are directly exposed to the inert Ar atmosphere during high-temperature calcination, which facilitates oxygen release and drives the phase transformation. Based on this, the proposed

16163028, 0, Downloaded from https://advanced.onlinelibrary.wiley.com/doi/10.1002/adfm.76250 by Dongwook Han - Seoul National University Of , Wiley Online Library on [01/06/2026]. See the Terms and Conditions (https://onlinelibrary.wiley.com/terms-and-conditions) on Wiley Online Library for rules of use; OA articles are governed by the applicable Creative Commons License

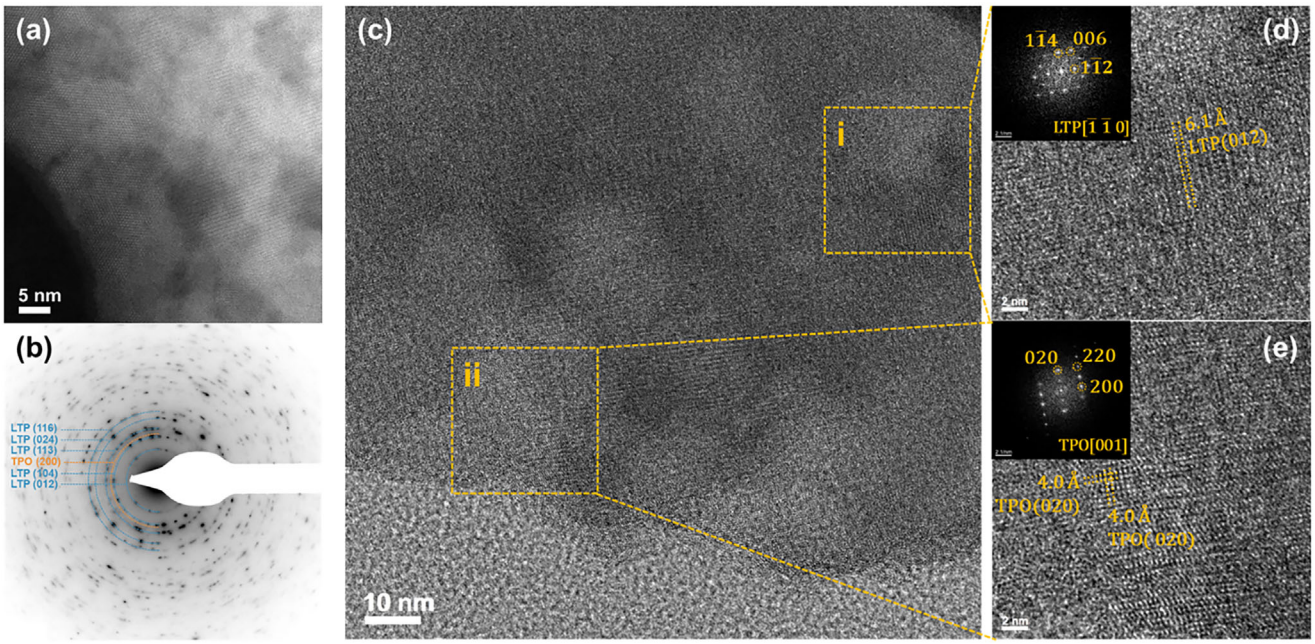

FIGURE 2 | Microstructural and crystallographic validation of the off-stoichiometric design. (a) STEM image and (b) corresponding SAED pattern of OS-LTP/C. (c) HR-TEM image, along with corresponding FFT patterns obtained from the (d) bulk and (e) subsurface regions, highlighting the distinct TPO domains.

synthesis reaction is described as follows: $LiTi_{2-\delta}(PO_4)_3 \rightarrow (1-2\delta)LiTi_2(PO_4)_3 + 3\delta TiP_2O_7 + \delta Li_2O\ (\uparrow) + \delta O_2\ (\uparrow)$, where the initial P/Ti atomic ratio corresponds to $3/(2-\delta)$. This predicted Li-loss is consistent with the Li-deficiency observed in the ICP-OES analysis.

Consequently, comprehensive multi-scale structural analyses (XRD, Rietveld refinement, STEM, and HR-TEM) provide compelling evidence that our off-stoichiometric engineering strategy has stabilized a unique hetero-architecture featuring a minor, functionally distinct TPO phase is intimately integrated within the primary LTP NASICON framework.

2.1.3 | Spectroscopic Analysis: Probing the Local Bonding Environment and Surface Chemistry

To probe the local chemical bonding structures and further validate the presence of the TPO secondary phase, Raman and Fourier-transform infrared (FT-IR) spectroscopies were employed. The Raman spectra of both P-LTP/C and OS-LTP/C (Figure 3a) display characteristic bands corresponding to the phosphate $(PO_4)^{3-}$ groups within the NASICON framework, including bending modes at ~434.6 and ~614.9 cm^{-1} and stretching modes at ~968.7 and ~1002.6 cm^{-1} [32]. Critically, the spectrum of OS-LTP/C exhibits a series of additional, distinct bands. These new features, such as vibrations from terminal PO_3 groups (e.g., ~1006.1 cm^{-1}) and P—O—P linkages (e.g., ~348.8 cm^{-1}), are the unambiguous vibrational fingerprints of the pyrophosphate $(P_2O_7)^{4-}$ groups in TPO, where a bridging oxygen connects two adjacent PO_4 tetrahedra [33, 34]. The existence of these P—O—P units was further corroborated by a characteristic FT-IR absorption band at ~752.2 cm^{-1} in the OS-LTP/C sample (Figure S3) [35, 36]. Accordingly, these spectroscopic results provide definitive, local-scale evidence for the TPO phase, perfectly complementing the long-range structural information obtained from the XRD and Rietveld refinement analyses.

The nature of the residual carbon, essential for improving the electronic conductivity of LTP, was also examined. The Raman spectra (Figure S4) show two prominent bands: the D-band (~1360 cm^{-1}) associated with disordered carbon and the G-band (~1590 cm^{-1}) related to graphitic carbon. The calculated intensity ratio (I_D/I_G) of ~1.04 for both samples indicates a predominantly amorphous carbonaceous character, which is further supported by a broad 2D band at ~2700 cm^{-1} [37].

X-ray photoelectron spectroscopy (XPS) was performed (Figure 3b–d). As hypothesized, the O 1s and P 2p core-level spectra for OS-LTP/C show a noticeable shift toward higher binding energies compared to P-LTP/C. This chemical shift is attributed to the higher covalency of the $(P_2O_7)^{4-}$ groups in the TPO domains [38, 39], which strengthens the P—O bonds and stabilizes the subsurface structure of LTP particles. Furthermore, quantitative deconvolution of the Ti 2p spectrum reveals a crucial change in the characteristic peak area ratios between the Ti^{4+} and Ti^{3+} states. Indeed, to maintain charge neutrality in the Ti-deficient lattice, the average oxidation state of titanium in OS-LTP/C is increased, resulting in a higher proportion of Ti^{4+} relative to Ti^{3+}. This is a significant advantage for its function as an anode: theoretically, a higher initial Ti^{4+} concentration provides more active sites for Li-ion insertion during charging. Thus, the XPS results reveal that our off-stoichiometric engineering not only creates a secondary phase but also strategically modifies the electronic structure of the host material to enhance both its stability and capacity.

16163028, 0, Downloaded from https://advanced.onlinelibrary.wiley.com/doi/10.1002/adfm.76250 by Dongwook Han - Seoul National University Of , Wiley Online Library on [01/06/2026]. See the Terms and Conditions (https://onlinelibrary.wiley.com/terms-and-conditions) on Wiley Online Library for rules of use; OA articles are governed by the applicable Creative Commons License

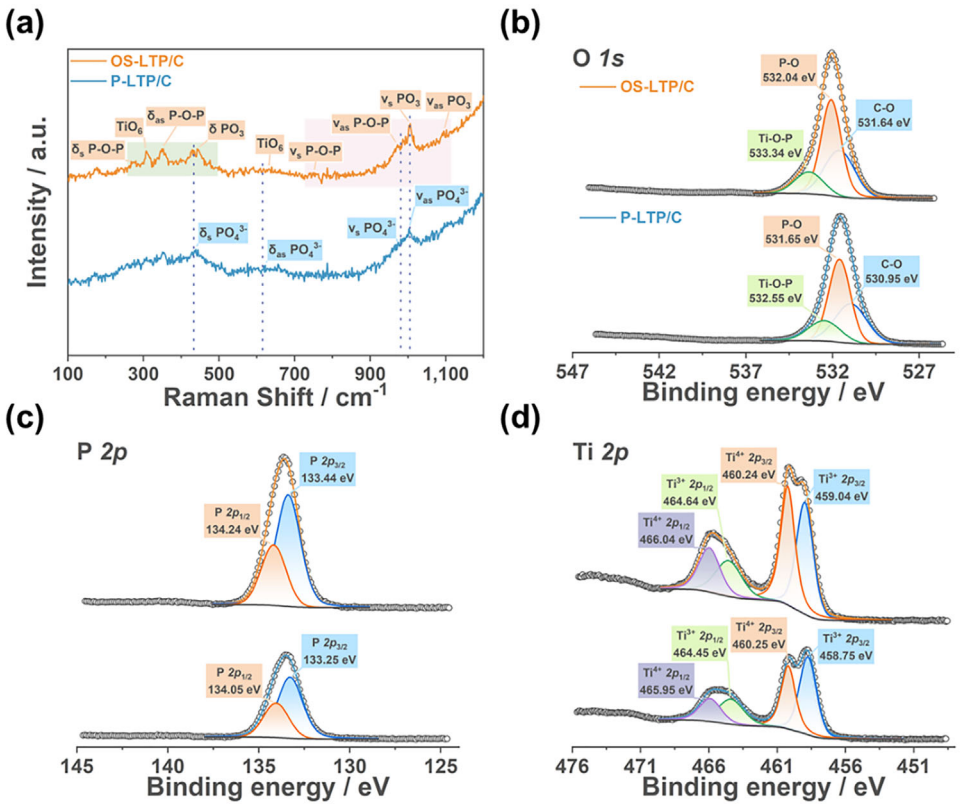

FIGURE 3 | Spectroscopic analysis of the local chemical and electronic structures. (a) Raman spectra of P-LTP/C and OS-LTP/C. High-resolution XPS spectra of the (b) O 1s, (c) P 2p, and (d) Ti 2p core levels for both samples.

2.2 | Electrochemical Performance

2.2.1 | Unlocking Ultrafast Charging Capability

The electrochemical behavior of the P-LTP/C and OS-LTP/C anodes was first investigated using galvanostatic charge/discharge cycling in half-cell configurations. The initial voltage profiles (Figure 4a) reveal subtle but significant differences. To deconvolve these features, differential capacity (dQ/dV) plots were analyzed (Figure 4b,c). Both materials display two primary redox couples at ~2.48 and ~2.78 V (vs. Li^+/Li), corresponding to the characteristic two-phase reactions of the Ti^{4+}/Ti^{3+} redox couple in the NASICON host [40]. Intriguingly, the OS-LTP/C anode exhibits an additional, well-defined redox peak at ~2.66 V, which is absent in its stoichiometric counterpart. This new electrochemical signature is attributed to the redox activity of the embedded TPO phase [26, 27], a conclusion strongly supported by in situ XRD analysis (Figure S5), which shows distinct structural evolution of this phase at a specific potential of ~2.6 V during cycling. The high covalency of the $(P_2O_7)^{4-}$ groups in TPO is believed to modulate the local electronic environment via an inductive effect, slightly elevating the redox potential of adjacent Ti sites and creating this new active center [41, 42].

Furthermore, as highlighted in the Introduction section, OS-LTP/C is expected to benefit from flexible lattice dynamics enabled by the rotational degrees of freedom in the flexible P—O—P bridges of TPO. In this context, sequential Pawley refinement of the in situ XRD patterns was performed to reveal the distinct structural evolution upon Li-ion extraction during discharging at 0.2C. In the early and middle stages of discharging (up to ~217 min), the TPO reflection at $2\theta \approx 22.5°$ is weakly visible, and the LTP peaks show merely minor shifts, indicating predominantly elastic lattice breathing. However, from the XRD patterns measured at 224 min onward, coinciding with the ~2.6 V redox region, the TPO reflection becomes clearly discernible, while the LTP peaks systematically shift toward higher 2θ, corresponding to lattice contraction due to the significant extraction of Li ions. This behavior suggests progressive structural ordering and strengthened interfacial coupling between the TPO domains and the LTP host of OS-LTP/C as the reaction proceeds. The absence of abrupt peak splitting or changes in symmetry further confirms that the NASICON framework remains crystallographically stable during cycling, supporting a strain-mediated rather than diffusion-mediated origin of the kinetic enhancement.

Next, the rate capability, a key metric for fast-charging performance, was systematically evaluated (Figure 4d). At a low C-rate of 0.1C, the OS-LTP/C delivered a slightly lower initial charge capacity (~125.4 mA h g^{-1}) than P-LTP/C (~130.6 mA h g^{-1}). This seemingly counterintuitive result is not related to the intrinsic material properties of LTP but rather to the slightly lower content of electrochemically active carbon in the OS-LTP/C composite (4.45 wt.% vs. 5.12 wt.% for P-LTP/C). As systematically verified by control experiments with varying carbon contents (Figure S6), the residual carbon contributes capacity primarily at low voltages with a sloping voltage profile. With both samples falling

16163028, 0, Downloaded from https://advanced.onlinelibrary.wiley.com/doi/10.1002/adfm.76250 by Dongwook Han - Seoul National University Of , Wiley Online Library on [01/06/2026]. See the Terms and Conditions (https://onlinelibrary.wiley.com/terms-and-conditions) on Wiley Online Library for rules of use; OA articles are governed by the applicable Creative Commons License

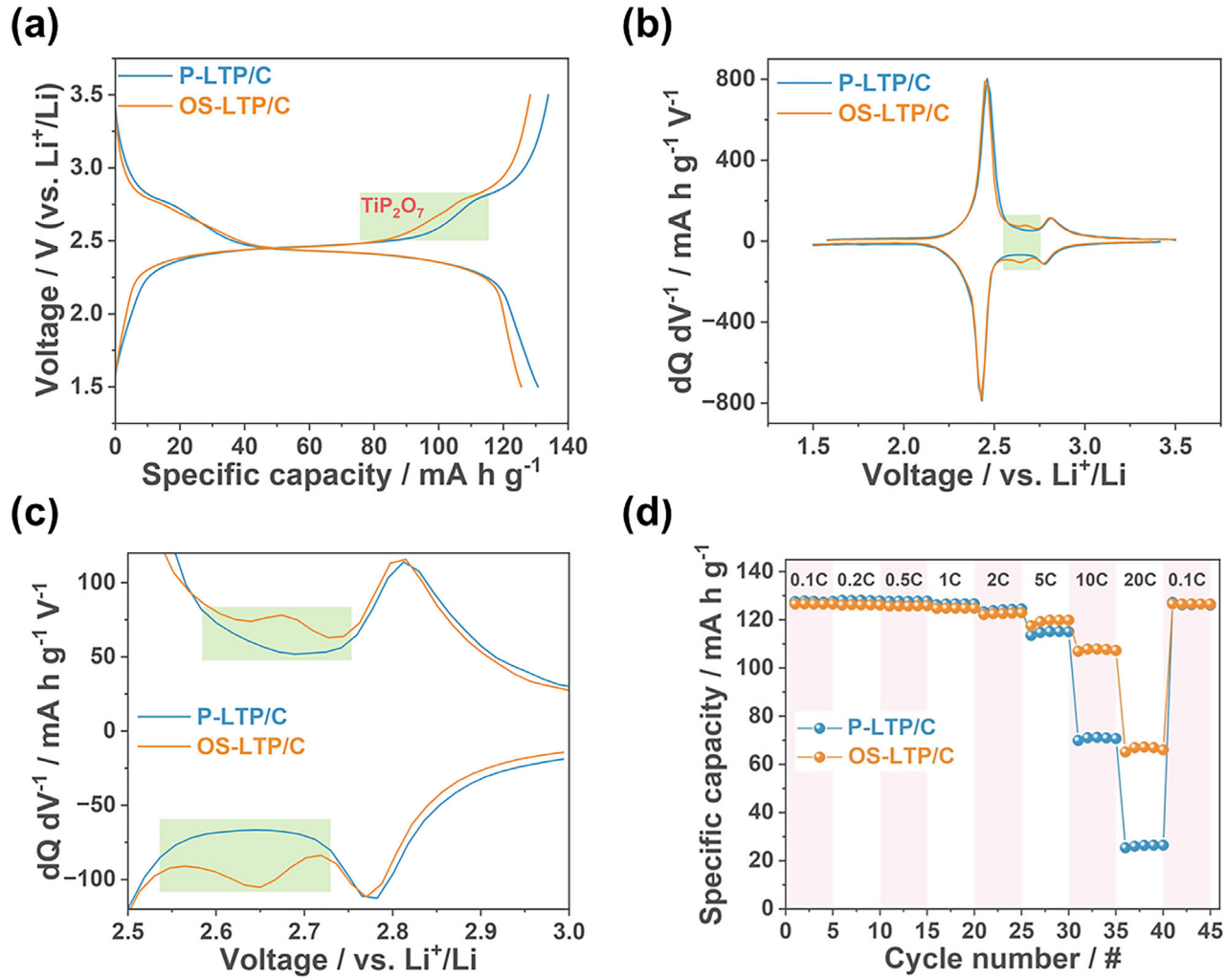

FIGURE 4 | Electrochemical performance and rate capability. (a) Initial galvanostatic charge/discharge profiles of P-LTP/C and OS-LTP/C at 0.1C. (b, c) Corresponding dQ/dV plots for P-LTP/C and OS-LTP/C. (d) Rate performance comparison.

slightly below the optimal carbon content range (~5–10 wt.%), the relatively lower carbon fraction in OS-LTP/C directly accounts for its slightly lower initial capacity compared to P-LTP/C at 0.1C.

The true advantage of our off-stoichiometric design becomes strikingly evident at high current densities. As the C-rate increases, a dramatic performance reversal occurs. While the charge capacity of P-LTP/C severely decays, OS-LTP/C demonstrates exceptional capacity retention. At a demanding rate of 10C, OS-LTP/C retains ~107.8 mA h g^{-1}, corresponding to an impressive ~86% of its initial capacity. This far exceeds the typical fast-charging benchmark of delivering ~80% capacity in 15 min (a 4C rate) [2]. More remarkably, even at an extreme 20C rate, OS-LTP/C sustains a significant capacity of ~67.2 mA h g^{-1}, whereas P-LTP/C delivers a negligible ~26.4 mA h g^{-1}. This outstanding high-rate performance is particularly noteworthy given the commercially relevant, microscale dimensions of the secondary particles (up to 30 μm), which typically impose severe kinetic limitations [1]. The persistent redox activity of the TPO phase across all C-rates (Figure S7) strongly suggests that these embedded domains act as kinetic gateways, facilitating rapid charge transfer and unlocking the ultrafast charging potential of the robust NASICON framework.

2.2.2 | Kinetic Analysis: Decoupling Bulk and Interfacial Contributions

To deconstruct the kinetic origins of the exceptional high-rate performance of OS-LTP/C, we employed the galvanostatic intermittent titration technique (GITT) and electrochemical impedance spectroscopy (EIS). The GITT analysis provides the first critical insight by decoupling bulk and interfacial kinetics. While OS-LTP/C consistently exhibits a significantly lower overall electrode resistance than P-LTP/C throughout charging, their bulk Li-ion diffusion coefficients (D_{Li+}) were found to be nearly identical, remaining in the range of 10^{-10} to 10^{-8} cm^2 s^{-1} (Figure 5a,b and Figure S8). This finding unambiguously indicates that the kinetic enhancement in OS-LTP/C does not stem from accelerated solid-state diffusion deep within the NASICON framework but must originate from processes occurring at or near the particle surface.

To precisely probe these interfacial and subsurface kinetics, EIS was conducted at different states of charge (SOC). The Nyquist plots (Figure 5c,d) were fitted using a standard equivalent circuit model that includes impedances for the Li-electrolyte interface (R_{ct}(Li)) and the LTP/C-electrolyte interface (R_{ct}(LTP/C)) [43]. While the R_{ct}(Li) values were comparable, the most dramatic

16163028, 0, Downloaded from https://advanced.onlinelibrary.wiley.com/doi/10.1002/adfm.76250 by Dongwook Han - Seoul National University Of , Wiley Online Library on [01/06/2026]. See the Terms and Conditions (https://onlinelibrary.wiley.com/terms-and-conditions) on Wiley Online Library for rules of use; OA articles are governed by the applicable Creative Commons License

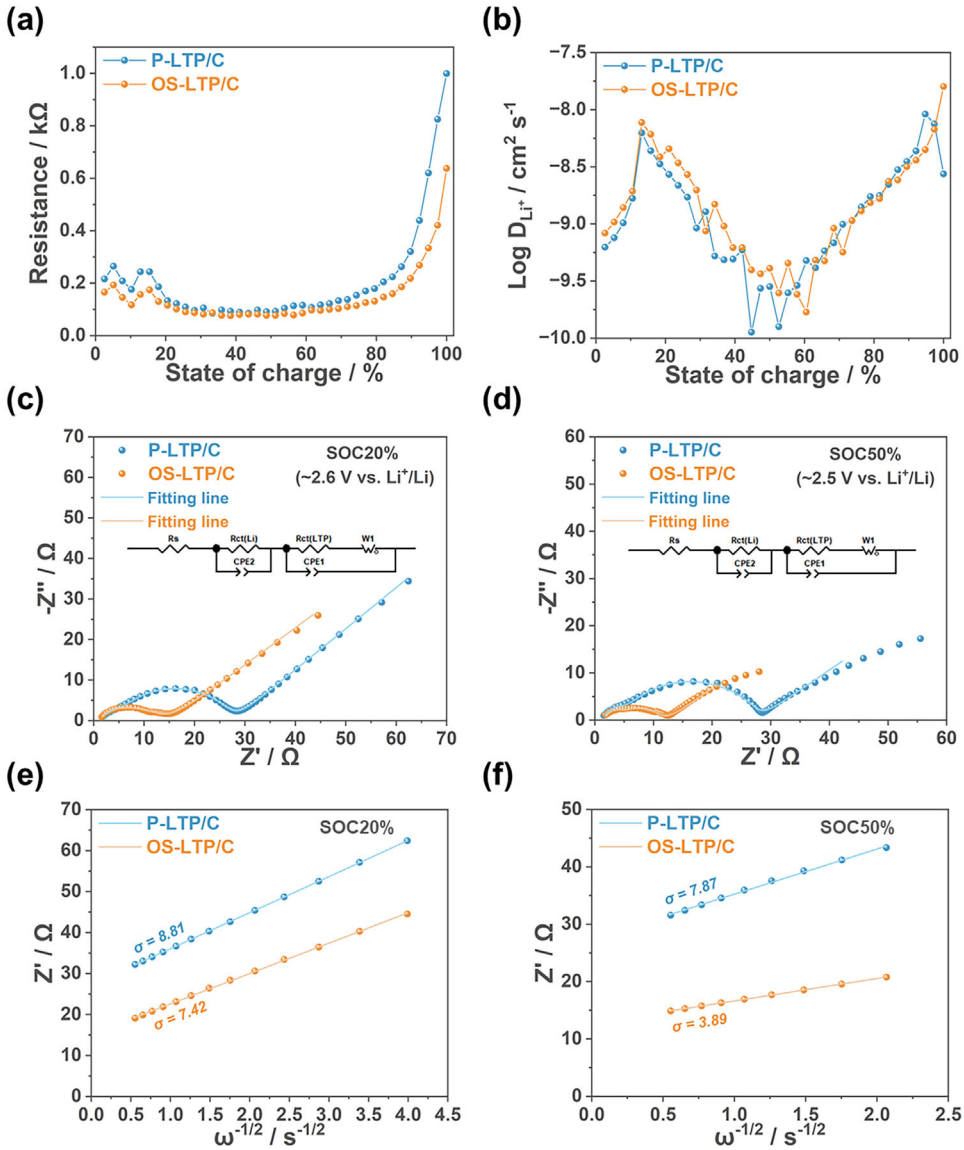

FIGURE 5 | Kinetic analysis of P-LTP/C and OS-LTP/C electrodes. (a) Effective electrode resistance and (b) Li-ion diffusion coefficients (D_{Li+}) calculated from GITT profiles as a function of SOC. Nyquist plots obtained from EIS measurements at (c) 20% and (d) 50% SOC, with the inset showing the equivalent circuit model used for fitting. Corresponding plots of Z′ vs. $\omega^{-1/2}$ in the low-frequency region measured at (e) 20% and (f) 50% SOC.

difference was observed in the charge-transfer resistance at the active material interface (Figure S9). The R_{ct}(LTP/C) value for the OS-LTP/C electrode was lower by a factor of approximately three than that of the P-LTP/C electrode at both 20% and 50% SOCs. This substantial reduction provides direct quantitative evidence that the embedded TPO domains fundamentally facilitate interfacial charge transfer.

Beyond the charge-transfer process, the low-frequency Warburg region of the impedance spectra offers further crucial insights into Li-ion transport within the particle subsurface. The Warburg coefficient (σ), which is inversely related to the square root of the diffusion coefficient [44], was calculated from the slope of Z′ vs. $\omega^{-1/2}$, where ω is the angular frequency ($\omega = 2\pi f$) (Figure 5e,f). At 20% SOC, the σ value for OS-LTP/C (~7.42 Ω $s^{-1/2}$) was significantly lower than for P-LTP/C (~8.81 Ω $s^{-1/2}$), indicating an approximately 1.4-fold enhancement in the Li-ion transport rate in the TPO-rich subsurface region. Surprisingly, this kinetic advantage in the subsurface becomes even more pronounced at higher SOCs, where the TPO phase is no longer redox-active. This suggests that the TPO domains create a highly conductive network for Li-ions near the surface, which remains effective throughout the entire charging process.

In summary, the off-stoichiometric engineering strategy creates integrated TPO domains that function as highly efficient kinetic gateways. While preserving the intrinsic bulk transport properties of the NASICON host, these domains (1) dramatically lower the activation barrier for interfacial charge transfer and (2) establish kinetically favorable transport pathways in the subsurface region, facilitated by the structural flexibility derived from the rotational degrees of freedom in the P—O—P bridges of TPO. This synergistic enhancement of surface and subsurface kinetics is the primary origin of the unlocked ultrafast charging capability in OS-LTP/C.

16163028, 0, Downloaded from https://advanced.onlinelibrary.wiley.com/doi/10.1002/adfm.76250 by Dongwook Han - Seoul National University Of , Wiley Online Library on [01/06/2026]. See the Terms and Conditions (https://onlinelibrary.wiley.com/terms-and-conditions) on Wiley Online Library for rules of use; OA articles are governed by the applicable Creative Commons License

2.2.3 | Theoretical Validation: Unraveling the Li-Ion Diffusion Landscape

To theoretically validate our experimental kinetic findings and gain atomistic insights into the Li-ion transport mechanism, we performed bond valence energy landscape (BVEL) calculations [45, 46]. This powerful computational tool maps the energy landscape for a mobile ion within a crystal lattice, revealing the most probable diffusion pathways and their associated energy barriers. The NASICON structure of LTP consists of a rigid 3D framework of corner-sharing TiO_6 octahedra and PO_4 tetrahedra, where Li-ions occupy 6-fold coordinated interstitial sites [21]. One might hypothesize that the slight lattice shrinkage observed in OS-LTP/C (Figure 6a,b and Table S1) could potentially hinder Li-ion transport.

The 3D BVEL isosurfaces for both P-LTP/C and OS-LTP/C, however, reveal a highly interconnected network of low-energy pathways, visually confirming that robust 3D diffusion channels are well-preserved in both structures (Figure 6c,d). To quantify the energetics of diffusion, we plotted the energy profile along the lowest-energy 1D migration pathway (Figure 6e,f) [47]. This reaction coordinate map identifies the stable interstitial sites (i1, i2) and the saddle points (s1, s5, s6) that represent the transition states. The energy difference between these sites defines the activation energy (E_a) for an ionic hop.

The calculations yield a noteworthy result: the activation energy for the primary 1D diffusion path is virtually identical for both materials, with E_a values of 0.405 eV for P-LTP/C and 0.404 eV for OS-LTP/C. While pathways requiring 2D or 3D diffusion (e.g., via the s6 transition state) exist, they involve significantly higher energy barriers (~0.72 eV) and are thus kinetically less favorable. Consistent with this, similar Li ionic conductivities were estimated for both P-LTP/C and OS-LTP/C from the BVEL calculations (Figure S10) [48]. The near-identical activation energies for the dominant diffusion channel and ionic conductivities, despite minor variations in their geometric paths, provide a profound theoretical explanation for our GITT results: the intrinsic bulk Li-ion diffusivity of the NASICON framework is fundamentally unaltered by the introduction of off-stoichiometry. We further revealed that while the stoichiometric TPO phase is essentially non-conductive due to the lack of viable diffusion pathways, the off-stoichiometric TPO phase (e.g., $Li_{0.15}Ti_{0.85}P_2O_{7-\delta}$) exhibits Li ionic conductivity comparable to that of the NASICON host (Figure S10).

Since BVEL interpretation indicates that the intrinsic bulk migration channels remain essentially unchanged regardless of the off-stoichiometry, the lattice contraction observed during the in situ XRD measurements (Figure S5) is likely to influence primarily the interfacial energetics rather than bulk diffusion. Under mechanical stress, the activation barrier for ion transfer is modified as follows: $\Delta E \approx \sigma \bullet \Omega$, where ΔE represents the stress-induced change in activation energy, σ is the local interfacial stress, and Ω is the activation volume associated with the transition state [49–53]. For typical interfacial stresses in oxide electrodes (10^2–10^3 MPa) and activation volumes of 1–5 Å^3, the stress-induced modulation of ΔE can reach 0.01–0.05 eV, a magnitude sufficient to measurably influence charge-transfer resistance. Within this stress–activation coupling framework, the dynamic electrochemical strain induced by Li-ion insertion/extraction modulates the interfacial charge-transfer barrier. The rotational flexibility of the P—O—P bridges in the TPO domains enables the elastic redistribution of the evolving strain field, thereby reducing local stress, lowering the effective interfacial activation energy, and preserving the three-dimensional NASICON diffusion network.

Therefore, these theoretical calculations corroborate our experimental evidence from GITT and EIS, leading to an unambiguous conclusion: the remarkable ultrafast charging capability unlocked in OS-LTP/C is not a bulk phenomenon. Instead, it is definitively attributed to the enhanced kinetics localized at the particle surface and subsurface.

2.2.4 | Mechanistic Insight: Quantifying the Pseudocapacitive Contribution

To provide the definitive mechanistic link between the embedded TPO domains and the enhanced high-rate performance, we quantified the contributions of diffusion-controlled and surface-capacitive processes to the total charge storage. Cyclic voltammetry (CV) was performed at various scan rates from 0.05 to 2 mV s^{-1} (Figure S11). First, the nature of the charge storage was assessed using the power-law relationship, $i_p = av^b$, where i_p is the peak current and v is the scan rate. The b-value, determined from the slope of the $\log(i_p)$ vs. $\log(v)$ plot, indicates the dominant mechanism: $b \approx 0.5$ signifies a diffusion-limited process, while $b \approx 1.0$ points to a surface-capacitive process. As plotted in Figure 7a,b, the calculated b-values for OS-LTP/C were consistently higher than those for P-LTP/C for both cathodic and anodic peaks, providing the initial qualitative evidence for an increased capacitive contribution.

To further deconvolve and precisely quantify these contributions, Dunn's method was applied, which separates the total current at a fixed potential into surface-capacitive (k_1v) and diffusion-controlled ($k_2v^{1/2}$) components [54]. As visualized in Figure 7c,d, the proportion of charge stored via surface-capacitive processes is substantially higher in OS-LTP/C across all scan rates. For instance, at a high scan rate of 2 mV s^{-1}, the capacitive contribution in OS-LTP/C reaches an impressive 78.3%, significantly larger than the 65.1% observed for P-LTP/C.

The strategic off-stoichiometric introduction of TPO is not merely a structural modification; it fundamentally imbues the anode with a significant pseudocapacitive character. This engineered pseudocapacitance acts as a highly efficient charge buffer at the electrode surface, enabling rapid charge acceptance and delivery. It is this mechanism that directly drives the exceptional high-rate capability and unlocks the ultrafast charging potential of the LTP-based anode.

2.2.5 | Long-Term Cyclability: Demonstrating Robust Structural Integrity

A critical prerequisite for any practical fast-charging anode is long-term operational stability under the severe structural strain induced by repeated, rapid Li-ion insertion/extraction. To

16163028, 0, Downloaded from https://advanced.onlinelibrary.wiley.com/doi/10.1002/adfm.76250 by Dongwook Han - Seoul National University Of , Wiley Online Library on [01/06/2026]. See the Terms and Conditions (https://onlinelibrary.wiley.com/terms-and-conditions) on Wiley Online Library for rules of use; OA articles are governed by the applicable Creative Commons License

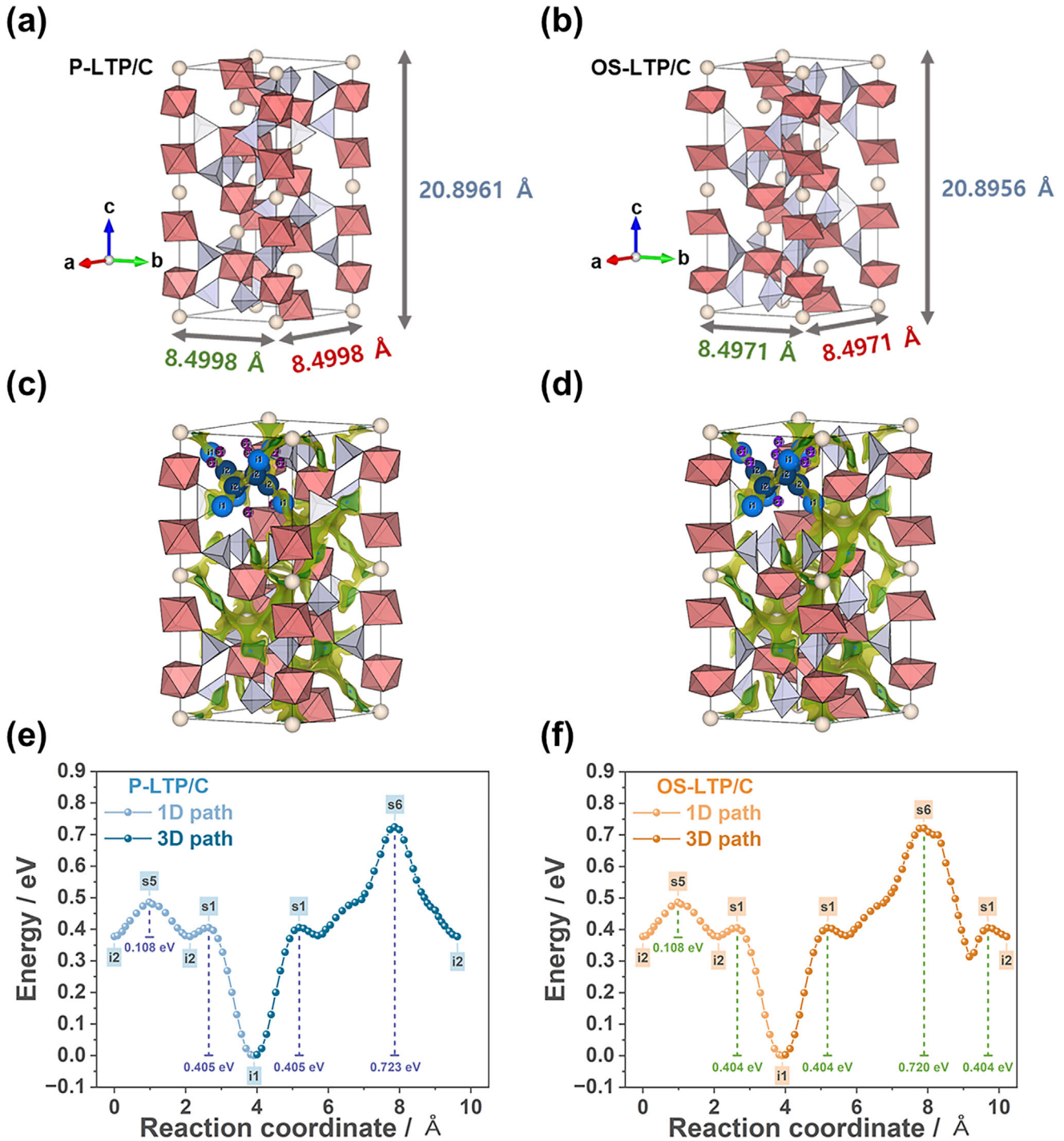

FIGURE 6 | Theoretical analysis of Li-ion diffusion pathways in LTP. Unit cells and refined lattice parameters of (a) P-LTP/C and (b) OS-LTP/C. 3D BVEL isosurfaces for Li-ion migration in (c) P-LTP/C and (d) OS-LTP/C, where green surfaces represent low-energy diffusion channels. 1D reaction coordinate plots showing the energy profile along the lowest-energy diffusion path for (e) P-LTP/C and (f) OS-LTP/C.

evaluate this, we first assessed the cyclability of both materials at a moderate rate of 0.1C (Figure 8a). Both P-LTP/C and OS-LTP/C exhibit exceptional stability, maintaining their initial charge capacities for over 100 cycles. This remarkable stability is corroborated by the negligible changes in their charge/discharge profiles and dQ/dV plots (Figure S12), signifying the excellent electrochemical reversibility of the host framework. Furthermore, ex situ XRD analysis confirms that the pristine NASICON crystal structure of both materials remains almost perfectly intact after 100 cycles, with no evidence of phase degradation (Figure 8b).

As illustrated in Figure 8c, unlike P-LTP/C, the OS-LTP/C anode demonstrates outstanding long-term durability even under a demanding charge rate of 10C, retaining a high specific capacity over 250 cycles. While the macroscopic cross-sectional morphologies of both electrodes appear similar, severe microstructural degradation was clearly observed in the P-LTP/C sample;

16163028, 0, Downloaded from https://advanced.onlinelibrary.wiley.com/doi/10.1002/adfm.76250 by Dongwook Han - Seoul National University Of , Wiley Online Library on [01/06/2026]. See the Terms and Conditions (https://onlinelibrary.wiley.com/terms-and-conditions) on Wiley Online Library for rules of use; OA articles are governed by the applicable Creative Commons License

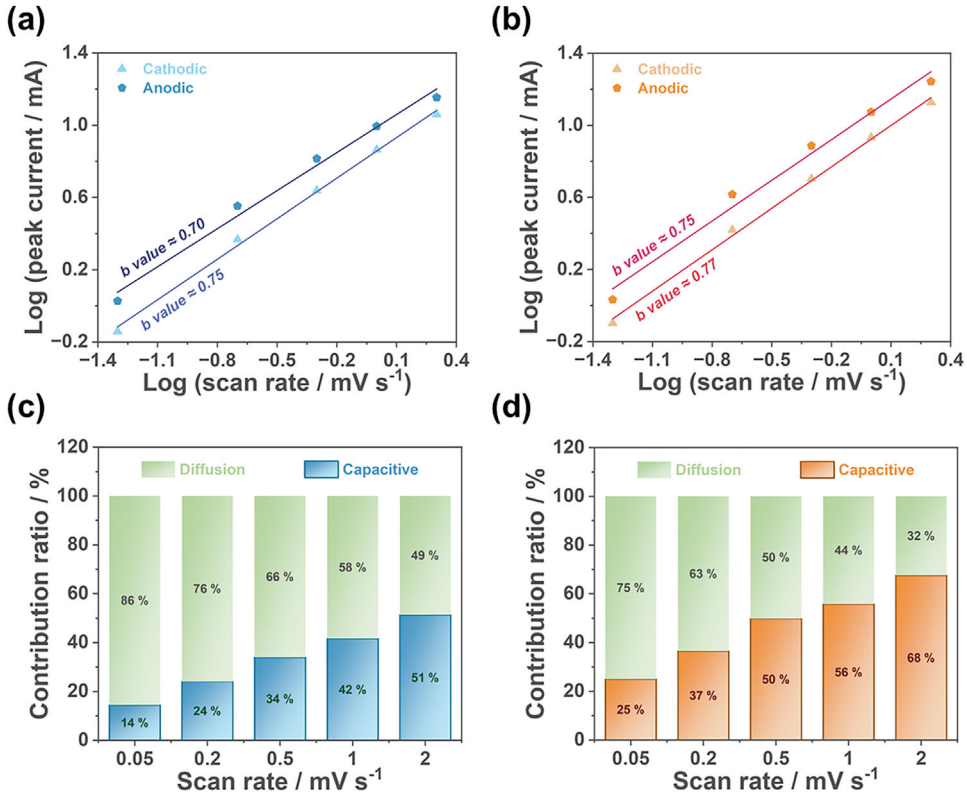

FIGURE 7 | Quantitative analysis of capacitive charge storage. Log(i_p) vs. log(v) plots for the cathodic and anodic peaks of (a) P-LTP/C and (b) OS-LTP/C. Comparison of capacitive contribution (shaded region) to the total current in (d) P-LTP/C and (d) OS-LTP/C at various scan rates from 0.05 to 2 mV s^{-1}.

long-range cracks and substantial amounts of unidentified residues were widespread within the microscale secondary particles of the P-LTP/C electrodes. By contrast, the structural integrity of the OS-LTP/C particles was well-preserved (Figure S13). In addition, even after 250 cycles at 10C, the O 1s and P 2p core-level spectra for OS-LTP/C maintain their noticeable peak shift toward higher binding energies compared to P-LTP/C (Figure S14). This persistent chemical shift indicates that the stronger P—O bonds associated with the TPO domains are retained, effectively preserving the robust subsurface structure of the LTP particles during long-term cycling.

In short, the superior cycling performance of OS-LTP/C is attributed to a powerful synergy enabled by our off-stoichiometric design: (1) the intrinsic structural integrity of the rigid NASICON host, which provides a robust scaffold against mechanical stress, and (2) the kinetically favorable TPO domains, which act as surface gateways to facilitate uniform Li-ion flux without active particle cracking. By preventing kinetic bottlenecks at the particle surface, these domains effectively mitigate localized stress accumulation and suppress degradation pathways, thereby preserving the material's integrity over extended high-power operation.

2.2.6 | Full-cell Applications: Practically Relevant Performance

To evaluate the practical viability of the OS-LTP/C anodes, $LiFePO_4$/C (LFP/C)||OS-LTP/C full cells were assembled. Detailed cell configurations and testing parameters are described in the Experimental section of the Supporting Information. Figure 9a presents the initial galvanostatic charge/discharge profiles of the LFP/C half cells, which deliver an initial discharge capacity of ~152 mA h g^{-1} at 0.2C. These half-cell data were utilized to determine the optimal N/P ratio and voltage window. Based on this optimization, the LFP/C||OS-LTP/C full cells exhibit a high initial discharge capacity (~143 mA h g^{-1}, based on the cathode mass) and an exceptional initial Coulombic efficiency of ~99.98% at 0.2C (Figure 9b), which is attributed to the minimized formation of unstable SEI layers on the anode and high reversibility of Li-ion insertion/extraction in both electrodes. Despite the inherently low operating voltage, these cells maintain excellent capacity retention (~96.8%) along with a high Coulombic efficiency (~99.93%) over 100 cycles (Figure 9c). Furthermore, the full cells demonstrate impressive rate capability, retaining ~63.2% of their 0.2C discharge capacity even at a high current density of 10C (Figure 9d).

To overcome the low-voltage issue, high-voltage ordered $LiNi_{0.5}Mn_{1.5}O_4$ (O-LNMO)||OS-LTP/C full cells were additionally demonstrated, and their cell specifications and initial charge/discharge profiles are shown in Figure S15. These full cells deliver a high initial discharge capacity (~129 mA h g^{-1}, based on the cathode mass) while operating at a moderate voltage of ~2.25 V. Consequently, the OS-LTP/C anodes possess universal compatibility, allowing them to be coupled with various commercial and upcoming cathodes, ranging from low-voltage LFP to high-voltage LNMO.

16163028, 0, Downloaded from https://advanced.onlinelibrary.wiley.com/doi/10.1002/adfm.76250 by Dongwook Han - Seoul National University Of , Wiley Online Library on [01/06/2026]. See the Terms and Conditions (https://onlinelibrary.wiley.com/terms-and-conditions) on Wiley Online Library for rules of use; OA articles are governed by the applicable Creative Commons License

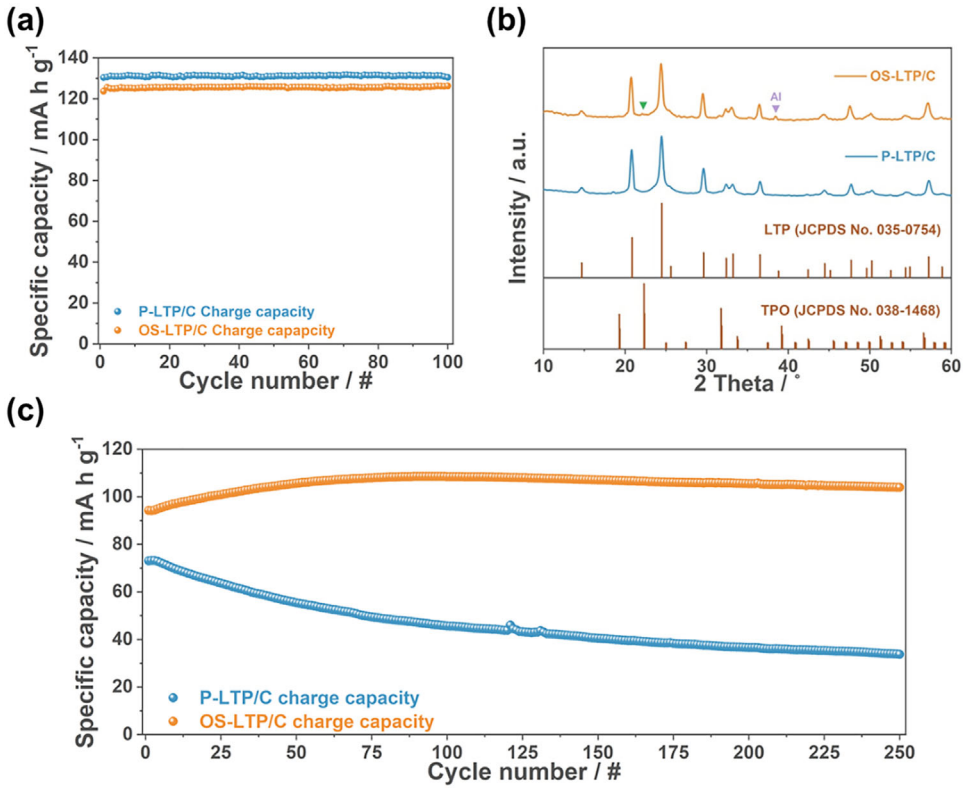

FIGURE 8 | Long-term cycling stability and structural integrity. (a) Cycling performance of P-LTP/C and OS-LTP/C at 0.1C. (b) Ex situ XRD patterns of both electrodes after 100 cycles. (c) High-rate, long-term cycling performance of P-LTP/C and OS-LTP/C at a charge rate of 10C (discharge at 0.2C) for 250 cycles.

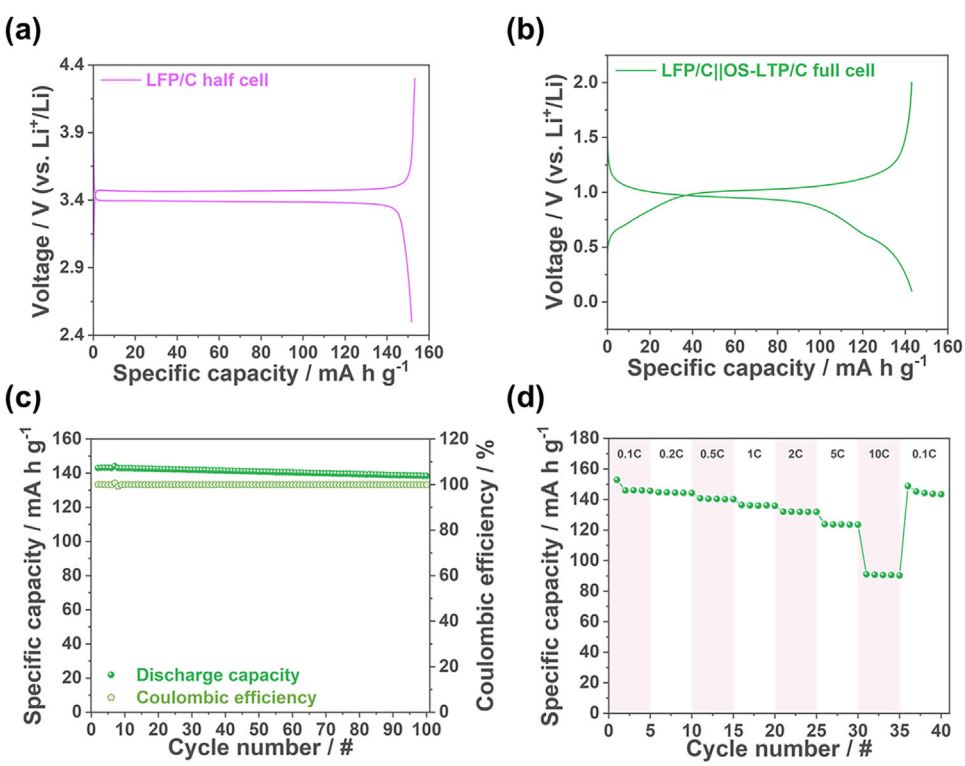

FIGURE 9 | Full-cell applications and performance. Initial galvanostatic charge/discharge profiles of (a) $LiFePO_4$/C (LFP/C) half cells and (b) LFP/C||OS-LTP/C full cells at 0.2C. (c) Cycling performance and (d) rate performance of the full cells.

16163028, 0, Downloaded from https://advanced.onlinelibrary.wiley.com/doi/10.1002/adfm.76250 by Dongwook Han - Seoul National University Of , Wiley Online Library on [01/06/2026]. See the Terms and Conditions (https://onlinelibrary.wiley.com/terms-and-conditions) on Wiley Online Library for rules of use; OA articles are governed by the applicable Creative Commons License

These applications confirm that our strategy not only unlocks ultrafast charging but also ensures the long-term reliability essential for next-generation energy storage applications, including all-solid-state batteries. This is because the robust structural integrity, intrinsic flexibility, and minimal volume change of the OS-LTP/C anode can effectively prevent mechanical degradation at the rigid solid-solid interface. Furthermore, the isostructural nature of our NASICON-based anode ensures exceptional chemical and crystallographic compatibility with widely used NASICON-type solid electrolytes (e.g., LATP), thereby potentially reducing the interfacial transfer resistance [55–57].

3 | Conclusion

In this work, we have established off-stoichiometric engineering as a powerful strategy to design a new class of ultrafast charging anodes, demonstrated through a novel $LiTi_2(PO_4)_3$/C composite featuring in situ embedded, pseudocapacitive TiP_2O_7 domains. Through a comprehensive investigation combining structural, spectroscopic, and electrochemical analyses, we elucidated a compelling, self-consistent mechanism: the integrated TiP_2O_7 domains act as highly efficient kinetic gateways. These domains do not alter the intrinsic, rapid bulk Li-ion diffusion of the robust NASICON framework but instead dramatically accelerate interfacial charge transfer and establish a kinetically favorable transport pathway in the subsurface region, thereby imbuing the material with a significant pseudocapacitive character.

This rationally designed hetero-architecture delivers an exceptional combination of high-rate capability and long-term stability. The resulting off-stoichiometric $LiTi_2(PO_4)_3$/C anode exhibited remarkable capacity retention at an extreme 10C rate and demonstrated outstanding durability over 250 cycles, which is particularly noteworthy for commercially relevant, microscale secondary particles reaching up to 30 μm ($D_{50} \approx 15$ μm). This work, therefore, not only presents a novel, high-performance anode material but also establishes off-stoichiometric engineering as a powerful and generalizable paradigm for designing next-generation, high-power electrodes. This design principle, creating built-in, functionally distinct domains to synergistically enhance surface and subsurface kinetics, is broadly applicable and holds significant promise for a wide range of future energy storage systems, including all-solid-state batteries and other polyanionic material systems.

4 | Experimental

4.1 | Synthesis of P-LTP/C and OS-LTP/C

Stoichiometric $LiTi_2(PO_4)_3$/C (P-LTP/C) and off-stoichiometric $LiTi_{2-\delta}(PO_4)_3$/C (OS-LTP/C) composites were synthesized via a citric acid-assisted sol–gel method. For P-LTP/C, two separate solutions were prepared. Solution A was formed by dissolving citric acid (0.5 mmol), lithium acetate (1 mmol), and titanium(IV) isopropoxide (2 mmol) in ethanol (90 mL). Solution B was prepared by dissolving ammonium dihydrogen phosphate (3 mmol) in deionized water (10 mL). Solution B was then added dropwise into Solution A under vigorous stirring. The resulting mixture was heated at 80°C for 2 h to form a viscous gel, which was subsequently dried in a vacuum oven at 80°C for 12 h. The obtained precursor powder was ground and then calcined at 800°C for 10 h under a flowing Ar atmosphere (2 L h^{-1}) to yield the final P-LTP/C product. For OS-LTP/C, an identical procedure was followed, except that the amount of the titanium precursor was reduced to achieve a target P/Ti atomic ratio of $3/(2-\delta)$, where $\delta = 0.05$.

4.2 | Materials Characterization

The phase purity and crystal structures of the synthesized powders were analyzed by X-ray diffraction (XRD; DE/D8 Advance, Bruker) using Cu Kα radiation ($\lambda = 1.5406$ Å). For quantitative structural analysis, high-resolution XRD data were collected (smartLAB, Rigaku) and subjected to Rietveld refinement using the TOPAS software package. To examine the detailed microstructure and crystallographic features, high-resolution transmission electron microscopy (HR-TEM) and scanning TEM (STEM) analyses were performed using a Titan 80–300 microscope (Thermo Fisher Scientific) operated at an accelerating voltage of 300 kV. Local bonding environments were probed by Raman spectroscopy (LabRAM HR, Horiba) with a 514 nm laser and Fourier-transform infrared spectroscopy (FT-IR; ALPHA-P, Bruker). Particle morphology and elemental distribution were examined using field-emission scanning electron microscopy (FE-SEM; SU8010, Hitachi) equipped with energy-dispersive X-ray spectroscopy (EDS). The particle size distributions were measured using a laser diffraction particle size analyzer (PSA; Mastersizer 3000, Malvern Panalytical). Precise elemental compositions were determined by inductively coupled plasma-optical emission spectrometry (ICP-OES; 5110 SVDV, Agilent), and carbon content was quantified with a CHNS/O elemental analyzer (FlashSmart, Thermo Fisher Scientific). Surface chemistry and elemental oxidation states were investigated by X-ray photoelectron spectroscopy (XPS; K-alpha+, Thermo Fisher Scientific), with all spectra calibrated to the C 1s peak at 284.8 eV. In situ and ex situ XRD analyses were performed to monitor structural changes during cycling. For in situ measurements, custom-modified CR2032 coin cells with X-ray transparent windows were used. For ex situ analysis, the cells were cycled 100 times at 0.1C and then carefully disassembled in an Ar-filled glovebox. Specifically, to obtain cross-sectional images, the extracted electrodes were milled using an ion-beam cross-section polisher (CP; IM4000plus CTC, Hitachi) prior to ex situ SEM observation.

4.3 | Theoretical Calculations

Bond valence energy landscape (BVEL) calculations were performed to map the Li-ion diffusion pathways using the softBV-GUI package [58, 59]. The initial crystal structure models for the calculations were derived from the crystallographic information files (CIFs) obtained from the Rietveld refinement of the experimental XRD data.

4.4 | Electrochemical Measurements

Working electrodes were fabricated by casting a slurry of the active material (P-LTP/C or OS-LTP/C, 80 wt.%), Super P carbon

16163028, 0, Downloaded from https://advanced.onlinelibrary.wiley.com/doi/10.1002/adfm.76250 by Dongwook Han - Seoul National University Of , Wiley Online Library on [01/06/2026]. See the Terms and Conditions (https://onlinelibrary.wiley.com/terms-and-conditions) on Wiley Online Library for rules of use; OA articles are governed by the applicable Creative Commons License

black (10 wt.%), and polyvinylidene fluoride (PVDF, 10 wt.%) in N-methyl-2-pyrrolidone (NMP) onto an Al foil current collector. After drying at 110°C under vacuum, 14 mm diameter circular electrodes were punched out. CR2032-type coin cells were assembled in an Ar-filled glovebox using the prepared electrodes, Li metal foil as the counter/reference electrode, and a 1 M $LiPF_6$ in EC/EMC/DMC (1:1:1 vol%) as the electrolyte. Galvanostatic charge/discharge tests were performed between 1.5 and 3.5 V (vs. Li^+/Li) using a battery cycler. A C-rate of 1C was defined as 100 mA g^{-1}. Rate capability was evaluated at various C-rates from 0.1C to 20C. Cyclic voltammetry (CV) was conducted on an Ivium-n-Stat potentiostat at scan rates from 0.05 to 2 mV s^{-1}. Electrochemical impedance spectroscopy (EIS) was also performed on the same instrument by applying an AC amplitude of 10 mV over a frequency range of 100 kHz to 0.01 Hz after charging the cells to a specific state of charge (SOC). The resulting impedance data were fitted using ZView software. The galvanostatic intermittent titration technique (GITT) was employed to determine key kinetic parameters. The active mass loadings of P-LTP/C and OS-LTP/C used for GITT analysis were 6.39 and 7.17 mg cm^{-2}, respectively. The measurement protocol involved applying a 20 min current pulse at 0.1C (corresponding to a specific current of 10 mA g^{-1}), followed by a 3 h relaxation period to allow the cell to reach a quasi-equilibrium state. This sequence was repeated throughout the charge process within the voltage window of 1.5–3.5 V. From the resulting voltage profiles, two parameters were extracted: (1) The effective electrode resistance was approximated from the instantaneous voltage drop (IR drop) at the beginning of the pulse and the overpotential (η) at the end of the pulse, where $R \approx |\eta|/i$. (2) The chemical diffusion coefficient of Li-ions (D_{Li+}) was calculated from the voltage response during the current pulse, assuming a Fick's second law-based diffusion model [60].

Acknowledgements

This study was financially supported by Seoul National University of Science and Technology (2024-0767) and also supported by Developing digital safety measurement to enhance the availability of smart structural monitoring of facilities, funded by Korea Research Institute of Standards and Science (KRISS – 2025 – GP2025 – 0009).

Conflicts of Interest

The authors declare no conflicts of interest.

Data Availability Statement

The data that support the findings of this study are available from the corresponding author upon reasonable request.

References

1. M. Weiss, R. Ruess, J. Kasnatscheew, et al., "Fast Charging of Lithium-Ion Batteries: A Review of Materials Aspects," *Advanced Energy Materials* 11 (2021): 2101126, https://doi.org/10.1002/aenm.202101126.

2. H. Xiao, J. Zhao, Q. Gao, et al., "Recent Advances in Fast-Charging Lithium-Ion Batteries: Mechanism, Materials, and Future Opportunities," *Chemical Engineering Journal* 506 (2025): 159927, https://doi.org/10.1016/j.cej.2025.159927.

3. Y. Liu, Y. Zhu, and Y. Cui, "Challenges and Opportunities Towards Fast-Charging Battery Materials," *Nature Energy* 4 (2019): 540.

4. W. Cai, Y.-X. Yao, G.-L. Zhu, et al., "A Review on Energy Chemistry of Fast-Charging Anodes," *Chemical Society Reviews* 49 (2020): 3806–3833, https://doi.org/10.1039/C9CS00728H.

5. Y. Dong, C. Liu, M. Rui, et al., "Review on Graphite Anodes for Fast-Charging Lithium-Ion Batteries: Mechanism, Modification and Characterizations," *Advanced Functional Materials* 35 (2025): 2506190, https://doi.org/10.1002/adfm.202506190.

6. Y. Liu, H. Shi, and Z.-S. Wu, "Recent Status, Key Strategies and Challenging Perspectives of Fast-Charging Graphite Anodes for Lithium-Ion Batteries," *Energy & Environmental Science* 16 (2023): 4834–4871, https://doi.org/10.1039/D3EE02213G.

7. S. Weng, G. Yang, S. Zhang, et al., "Kinetic Limits of Graphite Anode for Fast-Charging Lithium-Ion Batteries," *Nano-Micro Letters* 15 (2023): 215, https://doi.org/10.1007/s40820-023-01183-6.

8. S. A. Khan, I. Hussain, A. K. Thakur, et al., "Advancements in Battery Thermal Management System for Fast Charging/Discharging Applications," *Energy Storage Materials* 65 (2024): 103144, https://doi.org/10.1016/j.ensm.2023.103144.

9. A. Gupta and A. Manthiram, "Designing Advanced Lithium-Based Batteries for Low-Temperature Conditions," *Advanced Energy Materials* 10 (2020): 2001972, https://doi.org/10.1002/aenm.202001972.

10. P. Jia, J. Guo, Q. Li, et al., "Revisiting the kinetics enhancement strategies of Si anodes Through deconstructing particle–interface–electrode integration," *Energy & Environmental Science* 18 (2025): 2720–2746, https://doi.org/10.1039/D4EE05595K.

11. B. Zhao, R. Ran, M. Liu, and Z. Shao, "A Comprehensive Review of $Li_4Ti_5O_{12}$-Based Electrodes for Lithium-Ion Batteries: The Latest Advancements and Future Perspectives," *Materials Science and Engineering: R: Reports* 98 (2015): 1–71, https://doi.org/10.1016/j.mser.2015.10.001.

12. K. Kumar and R. Kundu, "Enlightenment of the Underestimated Parameters for a Fast-Charging Energy-Dense Anode for Lithium-Ion Batteries: An Outlook," *Energy & Fuels* 39 (2025): 8354–8368, https://doi.org/10.1021/acs.energyfuels.5c00335.

13. X. Zhang, J. Sun, Z. Cheng, M. Wu, Z. Guo, and H. Zhang, "Design, Perspective, and Challenge of Niobium-Based Anode Materials for High-Energy Alkali Metal-Ion Batteries," *Advanced Functional Materials* 34 (2024): 2405392, https://doi.org/10.1002/adfm.202405392.

14. S. Li, K. Wang, G. Zhang, et al., "Fast Charging Anode Materials for Lithium-Ion Batteries: Current Status and Perspectives," *Advanced Functional Materials* 32 (2022): 2200796, https://doi.org/10.1002/adfm.202200796.

15. X. Ding, Q. Zhou, X. Li, and X. Xiong, "Fast-Charging Anodes for Lithium Ion Batteries: Progress and Challenges," *Chemical Communications* 60 (2024): 2472–2488, https://doi.org/10.1039/D4CC00110A.

16. Y. Liu, W. Li, and Y. Xia, "Recent Progress in Polyanionic Anode Materials for Li (Na)-Ion Batteries," *Electrochemical Energy Reviews* 4 (2021): 447–472, https://doi.org/10.1007/s41918-021-00095-6.

17. J. Xiao, B. Zhang, J. Liu, et al., "NaSICON-Type Materials for Lithium-Ion Battery Applications: Progress and Challenges," *Nano Energy* 127 (2024): 109730, https://doi.org/10.1016/j.nanoen.2024.109730.

18. X. Wang, Z. Chen, S. Liu, et al., "Anode Interphase Design for Fast-Charging Lithium-Based Rechargeable Batteries," *Energy & Environmental Science* 18 (2025): 2648–2667, https://doi.org/10.1039/D4EE06107A.

19. R. Wang, L. Wang, R. Liu, X. Li, Y. Wu, and F. Ran, ""Fast-Charging" Anode Materials for Lithium-Ion Batteries From Perspective of Ion Diffusion in Crystal Structure," *ACS Nano* 18 (2024): 2611–2648, https://doi.org/10.1021/acsnano.3c08712.

20. P. N. Suryadi, J. Karunawan, O. Floweri, and F. Iskandar, "Toward High-Rate Capability of Intercalation Cathodes Li-Ion Batteries, Potency for Fast-Charging Application: A Materials Perspective," *Journal of Energy Storage* 68 (2023): 107634, https://doi.org/10.1016/j.est.2023.107634.

16163028, 0, Downloaded from https://advanced.onlinelibrary.wiley.com/doi/10.1002/adfm.76250 by Dongwook Han - Seoul National University Of , Wiley Online Library on [01/06/2026]. See the Terms and Conditions (https://onlinelibrary.wiley.com/terms-and-conditions) on Wiley Online Library for rules of use; OA articles are governed by the applicable Creative Commons License

21. B. Lang, B. Ziebarth, and C. Elsässer, "Lithium Ion Conduction in $LiTi_2(PO_4)_3$ and Related Compounds Based on the NASICON Structure: A First-Principles Study," *Chemistry of Materials* 27 (2015): 5040–5048, https://doi.org/10.1021/acs.chemmater.5b01582.

22. Z. Guo, Y. Zhang, S. Liu, et al., "Decorating Lithium Titanium-Phosphate Carbon Layers with Mo_2C as Efficient Li-Ion Storage Electrode," *ACS Applied Energy Materials* 6 (2023): 3724.

23. W. Sun, J. Liu, X. Liu, X. Fan, K. Zhou, and X. Wei, "Bimolecular-Induced Hierarchical Nanoporous $LiTi_2(PO_4)_3$ /C With Superior High-Rate and Cycling Performance," *Chemical Communications* 53 (2017): 8703–8706, https://doi.org/10.1039/C7CC04432A.

24. X. Jiang, H. Xu, H. Mao, J. Yang, and Y. Qian, "Surface-Disordered and Oxygen-Deficient $LiTi_{2-x}Mn_x(PO_{4-y})_3$ Nanoparticles for Enhanced Lithium-Ion Storage," *Journal of Power Sources* 320 (2016): 94–103, https://doi.org/10.1016/j.jpowsour.2016.04.078.

25. Z. Guo, X. Qin, Y. Xie, C. Lei, and T. W. Y. Zhang, "Advanced NASICON-type $LiTi_2(PO_4)_3$ as Electrode Materials for Lithium-Ion Batteries," *Chemical Physics Letters* 806 (2022): 140010, https://doi.org/10.1016/j.cplett.2022.140010.

26. F. A. Ali, A. M. Elseman, M. G. Fayed, A. M. Mohammad, and M. M. Rashad, "High-Yield Synthesis of TiP_2O_7 Nanopowders via a Facile Ball Milling Strategy for Enhanced Hybrid Supercapacitor Electrodes," *Journal of Energy Storage* 129 (2025): 117341, https://doi.org/10.1016/j.est.2025.117341.

27. S. S. Patil and P. S. Patil, "Transition Metal Pyrophosphate ($M_xP_2O_7$): A New Arrival in Hybrid Supercapacitors," *Chemical Engineering Journal* 455 (2023): 140639, https://doi.org/10.1016/j.cej.2022.140639.

28. C. S. Park, H. Kim, R. A. Shakoor, et al., "Anomalous Manganese Activation of a Pyrophosphate Cathode in Sodium Ion Batteries: A Combined Experimental and Theoretical Study," *Journal of the American Chemical Society* 135 (2013): 2787–2792, https://doi.org/10.1021/ja312044k.

29. A. Gezović, M. J. Vujković, M. Milović, V. Grudić, R. Dominko, and S. Mentus, "Recent Developments of $Na_4M_3(PO_4)_2(P_2O_7)$ as the Cathode Material for Alkaline-Ion Rechargeable Batteries: Challenges and Outlook"," *Energy Storage Materials* 37 (2021): 243.

30. R. Ramaraghavulu and S. Buddhudu, "Analysis of Structural, Thermal and Dielectric Properties of $LiTi_2(PO_4)_3$ Ceramic Powders," *Ceramics International* 37 (2011): 3651–3656, https://doi.org/10.1016/j.ceramint.2011.06.025.

31. Q. Hu, J.-Y. Liang, J.-Y. Liao, Z.-F. Tang, X. Ding, and C.-H. Chen, "A Comparative Study on Nanocrystalline Layered and Crystalline Cubic TiP_2O_7 for rechargeable Li/Na/K Alkali Metal Batteries," *Journal of Materials Chemistry A* 6 (2018): 15230–15236, https://doi.org/10.1039/C8TA05352A.

32. V. S. Kurazhkovskaya, D. M. Bykov, E. Y. Borovikova, N. Y. Boldyrev, L. Mikhalitsyn, and A. I. Orlova, "Vibrational Spectra and Factor Group Analysis of Lanthanide and Zirconium Phosphates $M^{III}_{0.33}Zr_2(PO_4)_3$, Where M^{III}=Y, La–Lu," *Vibrational Spectroscopy* 52 (2010): 137–143, https://doi.org/10.1016/j.vibspec.2009.12.002.

33. K. E. Lipinska-Kalita, M. B. Kruger, S. Carlson, and A. M. K. Andersen, "High-Pressure Studies of Titanium Pyrophosphate by Raman Scattering and Infrared Spectroscopy," *Physica B: Condensed Matter* 337 (2003): 221–229, https://doi.org/10.1016/S0921-4526(03)00407-1.

34. B. C. Cornilsen and R. A. Condrate Sr, "The Vibratonal Spectra of β-$Ca_2P_2O_7$ and γ-$Ca_2P_2O_7$," *Journal of Inorganic and Nuclear Chemistry* 41 (1979): 602–605, https://doi.org/10.1016/0022-1902(79)80457-1.

35. G. T. Stranford, R. A. Condrate Sr, and B. C. Cornilsen, "The Raman Spectrum of α-Zinc Pyrophosphate," *Journal of Molecular Structure* 73 (1981): 231–234, https://doi.org/10.1016/0022-2860(81)85067-3.

36. N. Khay and A. Ennaciri, "Vibrational Spectra of Double Diphosphates $CsLnP_2O_7$ (Ln=Gd, Tb, Dy, Ho, Y, Er, Tm, Yb)," *Journal of Alloys and Compounds* 323-324 (2001): 800–805, https://doi.org/10.1016/S0925-8388(01)01148-3.

37. R. Yuan, Y. Guo, I. Gurgan, et al., "Raman Spectroscopy Analysis of Disordered and Amorphous Carbon Materials: A Review of Empirical Correlations," *Carbon* 238 (2025): 120214, https://doi.org/10.1016/j.carbon.2025.120214.

38. R. Panigrahi and B. S. Mallik, "K Ions Migrate via a Cog-Wheel Mechanism in Solid Electrolyte Vanadium Pyrophosphates: Fact or Fiction?," *The Journal of Physical Chemistry C* 129 (2025): 16985–16998, https://doi.org/10.1021/acs.jpcc.5c03791.

39. G. Greczynski and L. Hultman, "X-Ray Photoelectron Spectroscopy: Towards Reliable Binding Energy Referencing," *Progress in Materials Science* 107 (2020): 100591, https://doi.org/10.1016/j.pmatsci.2019.100591.

40. L. Liu, T. Song, H. Han, et al., "Electrospun Sn-Doped $LiTi_2(PO_4)_3$ /C Nanofibers for Ultra-Fast Charging and Discharging," *Journal of Materials Chemistry A* 3 (2015): 10395–10402, https://doi.org/10.1039/C5TA00843C.

41. J. B. Goodenough and Y. Kim, "Challenges for Rechargeable Li Batteries," *Chemistry of Materials* 22 (2010): 587–603, https://doi.org/10.1021/cm901452z.

42. G. Oh, H. Kang, H. Park, et al., "Polyanionic-Based Cathode Materials for K-Ion Batteries," *Energy Storage Materials* 80 (2025): 104416, https://doi.org/10.1016/j.ensm.2025.104416.

43. A. C. Lazanas and M. I. Prodromidis, "Electrochemical Impedance Spectroscopy—A Tutorial," *ACS Measurement Science Au* 3 (2023): 162.

44. Y. Sun, L. Gai, Y. Zhou, X. Zuo, J. Zhou, and H. Jiang, "Polyhierarchically Structured TiP_2O_7/C Microparticles With Enhanced Electrochemical Performance for Lithium-Ion Batteries," *CrystEngComm* 16 (2014): 10681–10691, https://doi.org/10.1039/C4CE01547A.

45. L. L. Wong, K. C. Phuah, R. Dai, H. Chen, W. S. Chew, and S. Adams, "Bond Valence Pathway Analyzer—An Automatic Rapid Screening Tool for Fast Ion Conductors Within softBV," *Chemistry of Materials* 33 (2021): 625–641, https://doi.org/10.1021/acs.chemmater.0c03893.

46. S. Adams, "From Bond Valence Maps to Energy Landscapes for Mobile Ions in Ion-Conducting Solids," *Solid State Ionics* 177 (2006): 1625–1630, https://doi.org/10.1016/j.ssi.2006.03.054.

47. R. B. Nuernberg, J. F. Basbus, K. C. Lux, et al., "Correlation Between Structural Features and Ionic Transport in Lithium-Ion Conducting Glass–Ceramics From the $Li_{1+x}Cr_xGeTi_{1-x}(PO_4)_3$ System," *The Journal of Physical Chemistry C* 126 (2022): 4584–4592, https://doi.org/10.1021/acs.jpcc.1c09456.

48. S. Adams, "Origin of Fast Li^+-Ion Conductivity in the Compressible Oxyhalide $LiNbOCl_4$," *Energy Storage Materials* 68 (2024): 103359, https://doi.org/10.1016/j.ensm.2024.103359.

49. J. Maier, *Physical Chemistry of Ionic Materials: Ions and Electrons in Solids* (Wiley, 2004), https://doi.org/10.1002/0470020229.

50. J. Maier, "Ionic Conduction in Space Charge Regions," *Progress in Solid State Chemistry* 23 (1995): 171–263, https://doi.org/10.1016/0079-6786(95)00004-E.

51. J. Christensen and J. Newman, "Stress Generation and Fracture in Lithium Insertion Materials," *Journal of Solid State Electrochemistry* 10 (2006): 293–319, https://doi.org/10.1007/s10008-006-0095-1.

52. M. Z. Bazant, "Theory of Chemical Kinetics and Charge Transfer based on Nonequilibrium Thermodynamics," *Accounts of Chemical Research* 46 (2013): 1144–1160, https://doi.org/10.1021/ar300145c.

53. C. Monroe and J. Newman, "The Impact of Elastic Deformation on Deposition Kinetics at Lithium/Polymer Interfaces," *Journal of The Electrochemical Society* 152 (2005): A396, https://doi.org/10.1149/1.1850854.

54. V. Augustyn, P. Simon, and B. Dunn, "Pseudocapacitive Oxide Materials for High-Rate Electrochemical Energy Storage," *Energy & Environmental Science* 7 (2014): 1597–1614, https://doi.org/10.1039/c3ee44164d.

55. Z. Cui, S. Sun, G. Ning, et al., "Advances in the Application of First Principles Calculations to Phosphate-Based NASICON Battery

16163028, 0, Downloaded from https://advanced.onlinelibrary.wiley.com/doi/10.1002/adfm.76250 by Dongwook Han - Seoul National University Of , Wiley Online Library on [01/06/2026]. See the Terms and Conditions (https://onlinelibrary.wiley.com/terms-and-conditions) on Wiley Online Library for rules of use; OA articles are governed by the applicable Creative Commons License

Materials," *Journal of Materials Chemistry A* 12 (2024): 29335–29354, https://doi.org/10.1039/D4TA04943H.

56. J. Shen, C. Cui, J. Zhao, et al., "Advancing NASICON Solid-State Electrolytes for Lithium Metal Batteries: Interfacial Challenges, Engineering Strategies, and Future Directions," *Energy Storage Materials* 81 (2025): 104471, https://doi.org/10.1016/j.ensm.2025.104471.

57. S. Yu, A. Mertens, R. Schierholz, et al., "An Advanced All Phosphate Lithium-Ion Battery Providing High Electrochemical Stability, High Rate Capability and Long-Term Cycling Performance," *Journal of The Electrochemical Society* 164 (2017): A370–A379, https://doi.org/10.1149/2.1151702jes.

58. T. Runčevski, "Rietveld Refinement Practical Powder Diffraction Pattern Analysis using TOPAS. By Robert E. Dinnebier, Andreas Leineweber and John S. O. Evans. De Gruyter, 2019. Pp. 331. Price (paperback) EUR 69.95, USD 80.99, GBP 63.50. ISBN 978-3-11-045621-9, e-ISBN (PDF) 978-3-11-046138-1," *Journal of Applied Crystallography* 52 (2019): 1238–1239, https://doi.org/10.1107/S1600576719011178.

59. P. Thompson, D. E. Cox, and J. B. Hastings, "Rietveld Refinement of Debye–Scherrer Synchrotron X-Ray Data From Al_2O_3," *Journal of Applied Crystallography* 20 (1987): 79–83, https://doi.org/10.1107/S0021889887087090.

60. J. Kim, S. Park, S. Hwang, and W.-S. Yoon, "Principles and Applications of Galvanostatic Intermittent Titration Technique for Lithium-Ion Batteries," *Journal of Electrochemical Science and Technology* 13 (2022): 19–31, https://doi.org/10.33961/jecst.2021.00836.

Supporting Information

Additional supporting information can be found online in the Supporting Information section.

Supporting File: adfm76250-sup-0001-SuppMat.docx.

16163028, 0, Downloaded from https://advanced.onlinelibrary.wiley.com/doi/10.1002/adfm.76250 by Dongwook Han - Seoul National University Of , Wiley Online Library on [01/06/2026]. See the Terms and Conditions (https://onlinelibrary.wiley.com/terms-and-conditions) on Wiley Online Library for rules of use; OA articles are governed by the applicable Creative Commons License